Coherent Microwave-to-Optical Conversion via Six-Wave Mixing in Rydberg Atoms

Jingshan Han,[1] Thibault Vogt,[1,2] Christian Gross,[1] Dieter Jaksch,[3,1] Martin Kiffner,[1,3] and Wenhui Li[1,4,*]
[1]*Centre for Quantum Technologies, National University of Singapore, 3 Science Drive 2, Singapore 117543, Singapore*
[2]*MajuLab, CNRS-UNS-NUS-NTU International Joint Research Unit UMI 3654, Singapore 117543, Singapore*
[3]*Clarendon Laboratory, University of Oxford, Parks Road, Oxford OX1 3PU, United Kingdom*
[4]*Department of Physics, National University of Singapore, Singapore 117542, Singapore*

(Received 31 March 2017; revised manuscript received 18 November 2017; published 1 March 2018)

We present an experimental demonstration of converting a microwave field to an optical field via frequency mixing in a cloud of cold ^{87}Rb atoms, where the microwave field strongly couples to an electric dipole transition between Rydberg states. We show that the conversion allows the phase information of the microwave field to be coherently transferred to the optical field. With the current energy level scheme and experimental geometry, we achieve a photon-conversion efficiency of ~0.3% at low microwave intensities and a broad conversion bandwidth of more than 4 MHz. Theoretical simulations agree well with the experimental data, and they indicate that near-unit efficiency is possible in future experiments.

DOI: 10.1103/PhysRevLett.120.093201

Coherent and efficient conversion from microwave and terahertz radiation into optical fields and vice versa has tremendous potential for developing next-generation classical and quantum technologies. For example, these methods would facilitate the detection and imaging of millimeter waves with various applications in medicine, security screening, and avionics [1–4]. In the quantum domain, coherent microwave-optical conversion is essential for realizing quantum hybrid systems [5], where spin systems or superconducting qubits are coupled to optical photons that can be transported with low noise in optical fibers [6]. The challenge in microwave-optical conversion is to devise a suitable platform that couples strongly to both frequency bands, which are separated by several orders of magnitude in frequency, and provides an efficient link between them. Experimental work on microwave-optical conversion has been based on ferromagnetic magnons [7], frequency mixing in Λ-type atomic ensembles [8–11], whispering-gallery resonators [12,13], or nanomechanical oscillators [14–16]. All of these schemes include cavities to enhance the coupling to microwaves. The realization of near-unit conversion efficiencies as, e.g., required for transmitting quantum information remains an outstanding and important goal. Recently, highly excited Rydberg atoms have been identified as a promising alternative [17,18], as they feature strong electric dipole transitions in a wide frequency range from microwaves to terahertz [19].

In this Letter, we demonstrate coherent microwave-to-optical conversion of classical fields via six-wave mixing in Rydberg atoms. Because of the strong coupling of millimeter waves to Rydberg transitions, the conversion is realized in free space. In contrast to millimeter-wave induced optical fluorescence [20], frequency mixing is employed here to convert a microwave field into a unidirectional single frequency optical field. The long lifetime of Rydberg states allows us to make use of electromagnetically induced transparency (EIT) [21], which significantly enhances the conversion efficiency [22]. A free-space photon-conversion efficiency of 0.3% with a bandwidth of more than 4 MHz is achieved with our current experimental geometry. Optimized geometry and energy level configurations should enable the broadband interconversion of microwave and optical fields with near-unit efficiency [17]. Our results, thus, constitute a major step towards using Rydberg atoms for transferring quantum states between optical and microwave photons.

The energy levels for the six-wave mixing are shown in Fig. 1(a), and the experimental setup is illustrated in Fig. 1(b). The conversion of the input microwave field M into the optical field L is achieved via frequency mixing with four input auxiliary fields P, C, A, and R in a cold atomic cloud. Starting from the spin polarized ground state $|1\rangle$, the auxiliary fields and the microwave field M, all of which are nearly resonant with the corresponding atomic transitions, create a coherence between the states $|1\rangle$ and $|6\rangle$. This induces the emission of the light field L with frequency $\omega_L = \omega_P + \omega_C - \omega_A + \omega_M - \omega_R$ such that the resonant six-wave mixing loop is completed, where ω_X is the frequency of field X ($X \in \{P, R, M, C, L, A\}$). The emission direction of field L is determined by the phase matching condition $\mathbf{k}_L = \mathbf{k}_P + \mathbf{k}_C - \mathbf{k}_A + \mathbf{k}_M - \mathbf{k}_R$, where $\mathbf{k}_X$ is the wave vector of the corresponding field. The wave vectors of the microwave fields $\mathbf{k}_A$ and $\mathbf{k}_M$ are negligible, since they are much smaller than those of the optical fields and, to an excellent approximation, they cancel each other. Moreover, we have $\mathbf{k}_C \approx \mathbf{k}_R$, thus the converted light field L propagates in the same direction as the input field P. The transverse profile of the converted

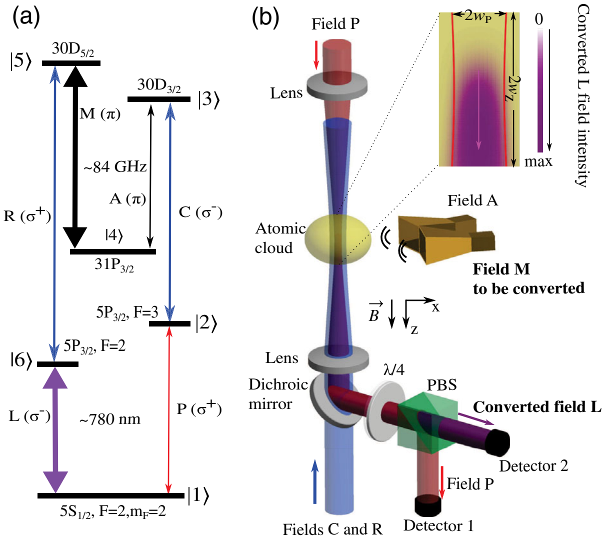

FIG. 1. (a) Relevant energy levels of a ^{87}Rb atom coupled by six nearly-resonant electromagnetic fields: $|1\rangle = |5S_{1/2}, F=2, m_F=2\rangle$, $|2\rangle = |5P_{3/2}, F=3, m_F=3\rangle$, $|3\rangle = |30D_{3/2}, m_J=1/2\rangle$, $|4\rangle = |31P_{3/2}, m_J = 1/2\rangle$, $|5\rangle = |30D_{5/2}, m_J=1/2\rangle$, and $|6\rangle = |5P_{3/2}, F = 2, m_F = 1\rangle$. Polarizations of the fields are indicated in brackets. The microwave field M ($\approx$84 GHz) is converted to the light field L ($\approx$780 nm) by six-wave mixing. (b) Experimental setup. Auxiliary light fields P, C, and R propagate collinearly along the z axis. They are focused onto the center of a Gaussian-distributed atomic cloud. The fields M and A are emitted from horn antennas enclosing an angle of 20°, and propagate horizontally. The bias magnetic field B along z defines the quantization axis. The copropagating fields L and P are separated by a polarization splitter ($\lambda/4$ + PBS) and detected simultaneously with avalanche photodiodes. The inset shows the simulated intensity and beam profile of the L field.

light field L resembles that of the auxiliary field P due to pulse matching [23,24] as illustrated in Fig. 1(b).

An experimental measurement begins with the preparation of a cold cloud of ^{87}Rb atoms in the $|5S_{1/2}, F = 2, m_F = 2\rangle$ state in a magnetic field of 6.1 G, as described previously in [25]. At this stage, the atomic cloud has a temperature of about 70 μK, a $1/e^2$ radius of $w_z = 1.85(10)$ mm along the z direction and a peak atomic density $n_0 = 2.1(2) \times 10^{10}$ cm^{-3}. We then switch on all of the input laser and microwave fields simultaneously for frequency mixing. The beams for both C and R fields are derived from a single 482 nm laser, while that of the P field comes from a 780 nm laser, and the two lasers are frequency locked to a single high-finesse temperature stabilized Fabry-Perot cavity [25]. The $1/e^2$ beam radii of these Gaussian fields at the center of the atomic cloud are $w_P = 25(1)$ μm, $w_C = 54(2)$ μm, and $w_R = 45(1)$ μm, respectively, and their corresponding peak Rabi frequencies are $\Omega_P^{(0)} = 2\pi \times 1.14(7)$ MHz, $\Omega_C^{(0)} = 2\pi \times 9.0(5)$ MHz, and $\Omega_R^{(0)} = 2\pi \times 6.2(3)$ MHz. The two microwave fields M and A, with a frequency separation of around 450 MHz, are generated by two different microwave sources via frequency multiplication. They are emitted from two separate horn antennas and propagate in the horizontal plane through the center of the atomic cloud, as shown in Fig. 1(b). The Rabi frequencies Ω_M and Ω_A are approximately uniform across the atomic cloud volume that intersects the laser beams. The Rabi frequency of the A field is $\Omega_A = 2\pi \times 1.0(1)$ MHz, while the Rabi frequency of the M field Ω_M is varied in different measurements. The details of the microwave Rabi frequency calibrations are presented in [26]. The P and L fields that emerge from the atomic cloud are collected by a diffraction-limited optical system [25], and they are separated using a quarter-wave plate and a polarization beam splitter (PBS). Their respective powers are measured with two different avalanche photodiode detectors. Each optical power measurement is an average of the recorded time-dependent signal in the range from 6 to 16 μs after switching on all the fields simultaneously, where the delay ensures the steady state is fully reached.

We experimentally demonstrate the coherent microwave-to-optical conversion via the six-wave mixing process by two measurements. First, we scan the detuning Δ_P of the P field across the atomic resonance and measure the power of the transmitted field P (P_P) and the power of the converted optical field L (P_L) simultaneously. All other input fields are held on resonance. The results of this measurement are shown in Fig. 2(a), where the spectrum of the transmitted field P (red squares) exhibits a double peak structure.

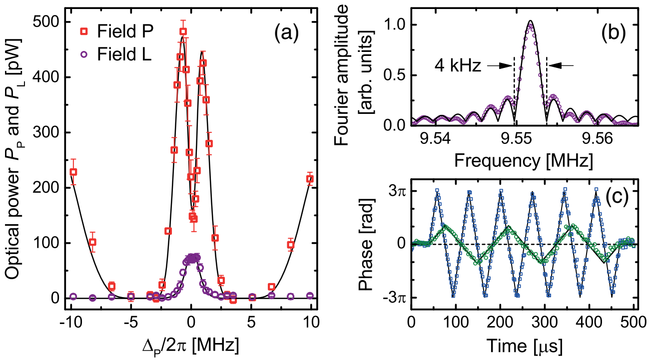

FIG. 2. (a) Spectra of fields P (red squares) and L (purple circles). The microwave field M has detuning $\Delta_M = 0$ and Rabi frequency $\Omega_M = 2\pi \times 1.25(12)$ MHz. The error bars indicate the standard deviation of five measurements. The solid curves are obtained from our theoretical model. (b) The Fourier-transformation of the optical heterodyne signal between the L field and a reference optical field for a pulse duration of 500 μs. The frequency difference between the two fields is $f_c = 9.5517$ MHz. The solid line shows the fit of a |sinc| function to the data. (c) The relative phase of the heterodyne signals for a phase modulated M field. Triangular modulations of 7 kHz and π amplitude (green circles) and of 14 kHz and 3π amplitude (blue squares) are shown. The phase is extracted by numerically demodulating the heterodyne signals [26]. The solid lines show the input phase modulation of the M field.

The signature of the six-wave mixing process is the converted field L (purple circles), and its spectrum features a pronounced peak around $\Delta_P = 0$.

Second, to verify the coherence of the conversion, we perform optical heterodyne measurements between the L field and a reference field that is derived from the same laser as the P field. Figure 2(b) shows that the Fourier spectrum of a 500 μs long beat note signal has a transform-limited sinc function dependence. The central frequency of the spectrum confirms that the frequency of the converted field L is determined by the resonance condition for the six-wave mixing process. Furthermore, we phase modulate the M field with a triangular modulation function and observe the recovery of the phase modulation in the optical heterodyne measurements, as shown in Fig. 2(c). This demonstrates that the phase information is coherently transferred in the conversion, as expected for a nonlinear frequency mixing process.

We simulate the experimental spectra by modeling the interaction of the laser and microwave fields with the atomic ensemble within the framework of coupled Maxwell-Bloch equations [26]. The time evolution of the atomic density operator ϱ is given by a Markovian master equation ($\hbar$ is the reduced Planck constant),

$$\partial_t \varrho = -\frac{i}{\hbar}[H, \varrho] + \mathcal{L}_\gamma \varrho + \mathcal{L}_{\mathrm{deph}} \varrho, \tag{1}$$

where H is the Hamiltonian describing the interaction of an independent atom with the six fields, and the term $\mathcal{L}_\gamma \varrho$ describes the spontaneous decay of the excited states. The last term, $\mathcal{L}_{\mathrm{deph}} \varrho$ in Eq. (1), accounts for dephasing of atomic coherences involving the Rydberg states $|3\rangle$, $|4\rangle$, and $|5\rangle$ with the dephasing rates γ_d, γ_{DD}, and $\gamma_{d'}$, respectively [26]. The sources of decoherence are the finite laser linewidths, atomic collisions, and dipole-dipole interactions between Rydberg atoms. The dephasing rates affect the P and L spectra and are found by fitting the steady state solution of coupled Maxwell-Bloch equations to the experimental spectra in Fig. 2(a). All other parameters are taken from independent experimental measurements and calibrations. We obtain $\gamma_d = 2\pi \times 150$ kHz, $\gamma_{DD} = 2\pi \times 150$ kHz and $\gamma_{d'} = 2\pi \times 560$ kHz and keep these values fixed in all simulations.

The system in Eq. (1) exhibits an approximate dark state [26],

$$|D\rangle \propto (\Omega_M^* \Omega_C^* |1\rangle - \Omega_M^* \Omega_P |3\rangle + \Omega_A^* \Omega_P |5\rangle), \tag{2}$$

for $\Omega_L/\Omega_P = -\Omega_A^* \Omega_R^* / (\Omega_M^* \Omega_C^*)$, where Ω_L is the Rabi frequency of field L. This state has a nonzero population only in metastable states $|1\rangle$, $|3\rangle$, and $|5\rangle$, and it is decoupled from all of the fields. The population in $|D\rangle$ increases with the buildup of the converted light field along the z direction, and thus, P_L saturates when all atoms are trapped in this state. Figure 3 shows the dependence of the output power P_L on the optical depth $D_P \propto n_0 w_z$ of the atomic cloud, and the theory curve agrees well with the experimental data. The predicted saturation at $D_P \approx 20$ is consistent with the population in $|D\rangle$ exceeding 99.8% at this optical depth.

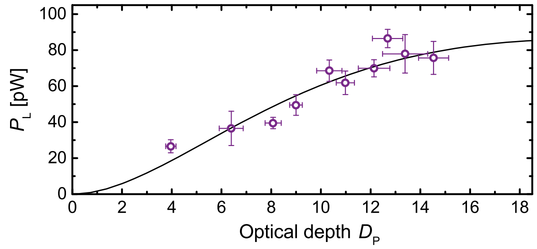

FIG. 3. P_L vs optical depth D_P, with all fields on resonance. D_P is varied by changing n_0, and the other conditions are the same as for Fig. 2(a). The circles are experimental data, and the solid line is the theoretically simulated curve. The error bars correspond to the standard deviation of four measurements.

Next, we analyze the dependence of the conversion process on detuning and intensity of the microwave field M. All auxiliary fields are kept on resonance and at constant intensity. Figure 4(a) shows P_L as a function of the microwave detuning Δ_M. We find that the spectrum of the L field can be approximated by a squared Lorentzian function centered at $\Delta_M = 0$, and its full width at half maximum (FWHM) is ≈ 6 MHz. The FWHM extracted from microwave spectra at different intensities I_M [38] is plotted in Fig. 4(b). The FWHM has a finite value >4 MHz in the low intensity limit, and it increases slowly with I_M due to power broadening. This large bandwidth is one of the distinguishing features of our scheme, and it is

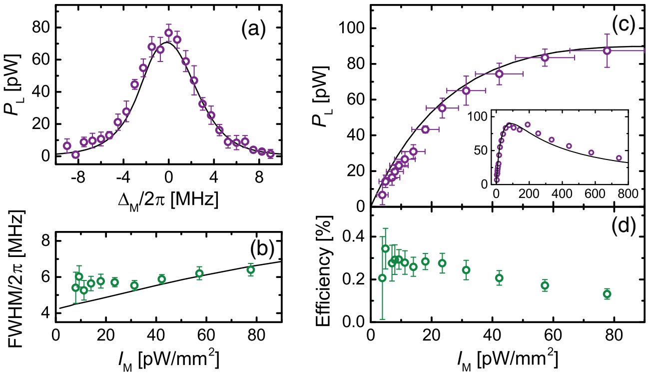

FIG. 4. (a) The spectrum of P_L against microwave detuning Δ_M for $I_M = 42(8)$ pW/mm^2. (b) FWHM vs I_M. The FWHM is extracted by fitting a squared Lorentzian function to the spectra. (c) P_L as a function of M field intensity I_M. The inset shows P_L over a much larger range of I_M. (d) The efficiency η calculated for the data shown in (c). The circles represent experimental data and solid curves simulation results. The vertical error bars in (a) and (c) correspond to the standard deviation of 4–6 measurements, and in (b) to the errors from fitting. The horizontal error bars in (c) are estimated uncertainties. The error bars in (d) are calculated from those in (c).

essential for extending the conversion scheme to the single-photon level [13]. In Fig. 4(c), we show measurements of P_L vs the intensity of the microwave field I_M at $\Delta_M = 0$. We find that the converted power P_L increases approximately linearly at low microwave intensities, and thus, our conversion scheme is expected to work in the limit of very weak input fields. The decrease of P_L at large intensities arises because the six-wave mixing process becomes inefficient if the Rabi frequency Ω_M is much larger than the Rabi frequency Ω_A of the auxiliary microwave. All of the theoretical curves in Fig. 4 agree well with the experimental data.

We evaluate the photon-conversion efficiency of our setup by considering the cylindrical volume $\mathcal{V}$ where the atomic cloud and all six fields overlap. This volume has a diameter $\sim 2w_P$ and a length $\sim 2w_z$ [see Fig. 1(b)]. We define the conversion efficiency as

$$\eta = \frac{P_L/\hbar\omega_L}{I_M S_M/\hbar\omega_M}, \tag{3}$$

where $S_M = 4w_P w_z$ is the cross section of the volume $\mathcal{V}$ perpendicular to $\mathbf{k}_M$. The efficiency η gives the ratio of the photon flux in L leaving volume $\mathcal{V}$ over the photon flux in M entering $\mathcal{V}$. As shown in Fig. 4(d), the conversion efficiency is approximately $\eta \approx 0.3\%$ over a range of low intensities, and then it decreases with increasing I_M. Note that η in Eq. (3) is a measure of the efficiency of the physical conversion process in the Rydberg medium based on the microwave power $I_M S_M$ impinging on S_M. This power is smaller than the total power emitted by the horn antenna since the M field has not been focused on $\mathcal{V}$ in our setup.

The good agreement between our model and the experimental data allows us to theoretically explore other geometries. To this end, we consider that the microwave fields M and A are copropagating with the P field, and we assume that all other parameters are the same [26]. We numerically evaluate the generated light power $P_L^{\parallel}$ for this setup and calculate the efficiency $\eta^{\parallel}$ by replacing P_L with $P_L^{\parallel}$ and S_M with $S_M^{\parallel} = \pi w_P^2$ in Eq. (3). We find $\eta^{\parallel} \approx 26\%$, which is approximately two orders of magnitude larger than η. This increase is mostly due to the geometrical factor $S_M/S_M^{\parallel} \approx 91$, since $P_L^{\parallel} \sim P_L$. Note that such a value for $\eta^{\parallel}$ is consistent with the efficiency achieved by a similar near-resonance frequency mixing scheme in the optical domain [39].

In conclusion, we have demonstrated coherent microwave-to-optical conversion via a six-wave mixing process utilizing the strong coupling of electromagnetic fields to Rydberg atoms. We have established the coherence of the conversion by a heterodyne measurement and demonstrated a large bandwidth by measuring the generated light as a function of the input microwave frequency. Coherence and large bandwidth are essential for taking our scheme to the single-photon level and using it in quantum technology applications. Our results are in good agreement with theoretical simulations based on an independent-atom model, thus showing a limited impact of atom-atom interactions on our conversion scheme.

This work has focussed on the physical conversion mechanism in Rydberg systems and provides several possibilities for future studies and applications. Alkali-metal-atom transitions offer a wide range of frequencies in the optical and microwave domain with properties similar to those exploited in this work. For example, the conversion of a microwave field to telecommunication wavelengths is possible by switching to different optical transitions and/or using different atomic species [18,40,41], which makes our approach promising for classical and quantum communication applications. Moreover, it has been theoretically shown that bidirectional conversion with near-unit efficiency is possible by using a different Rydberg excitation scheme and well-chosen detunings of the auxiliary fields [17]. Such a nonlinear conversion with near-unit efficiency has only been experimentally realized in the optical domain [42]. Reaching this level of efficiency requires good mode matching between the millimeter waves and the auxiliary optical fields [17], which can be achieved either by tightly focusing the millimeter wave or by confining it to a waveguide directly coupled to the conversion medium [11,43]. Eventually, extending our conversion scheme to millimeter waves in a cryogenic environment [44,45] would pave the way towards quantum applications.

The authors thank Tom Gallagher for useful discussions and acknowledge the support by the National Research Foundation, Prime Minister's office, Singapore and the Ministry of Education, Singapore under the Research Centres of Excellence programme. This work is partly supported by Singapore Ministry of Education Academic Research Fund Tier 2 (Grant No. MOE2015-T2-1-085). M. K. would like to acknowledge the use of the University of Oxford Advanced Research Computing (ARC) facility [46].

---

[*] wenhui.li@nus.edu.sg

[1] A. J. L. Adam, Review of near-field terahertz measurement methods and their applications, J. Infrared Millim. Waves **32**, 976 (2011).

[2] W. L. Chan, J. Deibel, and D. M. Mittleman, Imaging with terahertz radiation, Rep. Prog. Phys. **70**, 1325 (2007).

[3] M. Tonouchi, Cutting-edge terahertz technology, Nat. Photonics **1**, 97 (2007).

[4] X. C. Zhang, A. Shkurinov, and Y. Zhang, Extreme terahertz science, Nat. Photonics **11**, 16 (2017).

[5] Z.-L. Xiang, S. Ashhab, J. Q. You, and F. Nori, Hybrid quantum circuits: Superconducting circuits interacting with other quantum systems, Rev. Mod. Phys. **85**, 623 (2013).

[6] H. J. Kimble, The quantum internet, Nature (London) **453**, 1023 (2008).

[7] R. Hisatomi, A. Osada, Y. Tabuchi, T. Ishikawa, A. Noguchi, R. Yamazaki, K. Usami, and Y. Nakamura, Bidirectional conversion between microwave and light via ferromagnetic magnons, Phys. Rev. B **93**, 174427 (2016).

[8] L. A. Williamson, Y.-H. Chen, and J. J. Longdell, Magneto-Optic Modulator with Unit Quantum Efficiency, Phys. Rev. Lett. **113**, 203601 (2014).

[9] C. O'Brien, N. Lauk, S. Blum, G. Morigi, and M. Fleischhauer, Interfacing Superconducting Qubits and Telecom Photons via a Rare-Earth-Doped Crystal, Phys. Rev. Lett. **113**, 063603 (2014).

[10] S. Blum, C. O'Brien, N. Lauk, P. Bushev, M. Fleischhauer, and G. Morigi, Interfacing microwave qubits and optical photons via spin ensembles, Phys. Rev. A **91**, 033834 (2015).

[11] M. Hafezi, Z. Kim, S. L. Rolston, L. A. Orozco, B. L. Lev, and J. M. Taylor, Atomic interface between microwave and optical photons, Phys. Rev. A **85**, 020302 (2012).

[12] D. V. Strekalov, H. G. L. Schwefel, A. A. Savchenkov, A. B. Matsko, L. J. Wang, and N. Yu, Microwave whispering-gallery resonator for efficient optical up-conversion, Phys. Rev. A **80**, 033810 (2009).

[13] A. Rueda, F. Sedlmeir, M. C. Collodo, U. Vogl, B. Stiller, G. Schunk, D. V. Strekalov, C. Marquardt, J. M. Fink, O. Painter, G. Leuchs, and H. G. L. Schwefel, Efficient microwave to optical photon conversion: An electro-optical realization, Optica **3**, 597 (2016).

[14] J. Bochmann, A. Vainsencher, D. D. Awschalom, and A. N. Cleland, Nanomechanical coupling between microwave and optical photons, Nat. Phys. **9**, 712 (2013).

[15] R. W. Andrews, R. W. Peterson, T. P. Purdy, K. Cicak, R. W. Simmonds, C. A. Regal, and K. W. Lehnert, Bidirectional and efficient conversion between microwave and optical light, Nat. Phys. **10**, 321 (2014).

[16] T. Bagci, A. Simonsen, S. Schmid, L. G. Villanueva, E. Zeuthen, J. Appel, J. M. Taylor, A. Sørensen, K. Usami, A. Schliesser *et al.*, Optical detection of radio waves through a nanomechanical transducer, Nature (London) **507**, 81 (2014).

[17] M. Kiffner, A. Feizpour, K. T. Kaczmarek, D. Jaksch, and J. Nunn, Two-way interconversion of millimeter-wave and optical fields in Rydberg gases, New J. Phys. **18**, 093030 (2016).

[18] B. T. Gard, K. Jacobs, R. McDermott, and M. Saffman, Microwave-to-optical frequency conversion using a cesium atom coupled to a superconducting resonator, Phys. Rev. A **96**, 013833 (2017).

[19] T. F. Gallagher, *Rydberg Atoms* (Cambridge University Press, Cambridge, 1994).

[20] C. G. Wade, N. Šibalić, N. R. de Melo, J. M. Kondo, C. S. Adams, and K. J. Weatherill, Real-time near-field terahertz imaging with atomic optical fluorescence, Nat. Photonics **11**, 40 (2017).

[21] A. K. Mohapatra, T. R. Jackson, and C. S. Adams, Coherent Optical Detection of Highly Excited Rydberg States Using Electromagnetically Induced Transparency, Phys. Rev. Lett. **98**, 113003 (2007).

[22] M. Fleischhauer, A. Imamoglu, and J. P. Marangos, Electromagnetically induced transparency: Optics in coherent media, Rev. Mod. Phys. **77**, 633 (2005).

[23] S. E. Harris, Electromagnetically Induced Transparency with Matched Pulses, Phys. Rev. Lett. **70**, 552 (1993).

[24] S. E. Harris, Normal Modes for Electromagnetically Transparency, Phys. Rev. Lett. **72**, 52 (1994).

[25] J. Han, T. Vogt, M. Manjappa, R. Guo, M. Kiffner, and W. Li, Lensing effect of electromagnetically induced transparency involving a Rydberg state, Phys. Rev. A **92**, 063824 (2015).

[26] See Supplemental Material at http://link.aps.org/supplemental/10.1103/PhysRevLett.120.093201, which also contains Refs. [27–37], for details about the theoretical model and the calibration of experimental parameters.

[27] J. Han, T. Vogt, and W. Li, Spectral shift and dephasing of electromagnetically induced transparency in an interacting Rydberg gas, Phys. Rev. A **94**, 043806 (2016).

[28] Wolfram Research, Inc., *Mathematica Version 10.1*, Wolfram Research, Inc., Irvine, 2015.

[29] D. A. Steck, Rubidium 87D Line Data, http://steck.us/alkalidata (revision 2.1.4, 23 December 2010).

[30] I. I. Beterov, I. I. Ryabtsev, D. B. Tretyakov, and V. M. Entin, Quasiclassical calculations of blackbody-radiation-induced depopulation rates and effective lifetimes of Rydberg nS, nP, and nD alkali-metal atoms with $n \leq 80$, Phys. Rev. A **79**, 052504 (2009).

[31] D. B. Branden, T. Juhasz, T. Mahlokozera, C. Vesa, R. O. Wilson, M. Zheng, A. Kortyna, and D. A. Tate, Radiative lifetime measurements of rubidium Rydberg states, J. Phys. B **43**, 015002 (2010).

[32] E. Arimondo, V coherent population trapping in laser spectroscopy, Prog. Opt. **35**, 257 (1996).

[33] M. Tanasittikosol, J. Pritchard, D. Maxwell, A. Gauguet, K. Weatherill, R. Potvliege, and C. Adams, Microwave dressing of Rydberg dark states, J. Phys. B **44**, 184020 (2011).

[34] G. Grynberg, A. Aspect,, and C. Fabre, *Introduction to Quantum Optics: From the Semi-Classical Approach to Quantized Light* (Cambridge University Press, Cambridge, 2010).

[35] J. A. Sedlacek, A. Schwettmann, H. Kübler, R. Löw, T. Pfau, and J. P. Shaffer, Microwave electrometry with Rydberg atoms in a vapour cell using bright atomic resonances, Nat. Phys. **8**, 819 (2012).

[36] C. L. Holloway, J. A. Gordon, A. Schwarzkopf, D. A. Anderson, S. A. Miller, N. Thaicharoen, and G. Raithel, Sub-wavelength imaging and field mapping via electromagnetically induced transparency and Autler-Townes splitting in Rydberg atoms, Appl. Phys. Lett. **104**, 244102 (2014).

[37] J. A. Gordon, C. L. Holloway, A. Schwarzkopf, D. A. Anderson, S. Miller, N. Thaicharoen, and G. Raithel, Millimeter wave detection via Autler-Townes splitting in rubidium Rydberg atoms, Appl. Phys. Lett. **105**, 024104 (2014).

[38] The intensity I_M is related to the Rabi frequency Ω_M by $I_M = \frac{1}{2}\varepsilon_0 c(\hbar\Omega_M/d_{45})^2$, where c is the speed of the light, ε_0 the electric constant, $\hbar$ the Planck constant, and d_{45} is the

electric dipole moment between states $|4\rangle$ and $|5\rangle$ (See Ref. [26]).

[39] A. J. Merriam, S. J. Sharpe, M. Shverdin, D. Manuszak, G. Y. Yin, and S. E. Harris, Efficient Nonlinear Frequency Conversion in an All-Resonant Double- Λ System, Phys. Rev. Lett. **84**, 5308 (2000).

[40] S. L. Gilbert, Frequency stabilization of a fiber laser to rubidium: A high-accuracy $1.53-\mu m$ wavelength standard, Proc. SPIE Int. Soc. Opt. Eng. **1837**, 146 (1993).

[41] M. A. Bouchiat, J. Guéna, P. Jacquier, M. Lintz, and L. Pottier, The cs 6s-7s-6p3/2 forbidden three-level system: analytical description of the inhibited fluorescence and optical rotation spectra, J. Phys. (Paris) **50**, 157 (1989).

[42] A. J. Merriam, S. J. Sharpe, H. Xia, D. Manuszak, G. Y. Yin, and S. E. Harris, Efficient gas-phase generation of coherent vacuum ultraviolet radiation, Opt. Lett. **24**, 625 (1999).

[43] S. D. Hogan, J. A. Agner, F. Merkt, T. Thiele, S. Filipp, and A. Wallraff, Driving Rydberg-Rydberg Transitions from a Coplanar Microwave Waveguide, Phys. Rev. Lett. **108**, 063004 (2012).

[44] C. Hermann-Avigliano, R. C. Teixeira, T. L. Nguyen, T. Cantat-Moltrecht, G. Nogues, I. Dotsenko, S. Gleyzes, J. M. Raimond, S. Haroche, and M. Brune, Long coherence times for Rydberg qubits on a superconducting atom chip, Phys. Rev. A **90**, 040502 (2014).

[45] D. Cano, H. Hattermann, B. Kasch, C. Zimmermann, R. Kleiner, D. Koelle, and J. Fortágh, Experimental system for research on ultracold atomic gases near superconducting microstructures Eur. Phys. J. D **63**, 17 (2011).

[46] http://dx.doi.org/10.5281/zenodo.22558.

Supplemental Material for
Coherent Microwave-to-Optical Conversion via Six-Wave Mixing in Rydberg Atoms

Jingshan Han[1], Thibault Vogt[1,2], Christian Gross[1], Dieter Jaksch[3,1], Martin Kiffner[1,3], and Wenhui Li[1,4]
Centre for Quantum Technologies, National University of Singapore, 3 Science Drive 2, Singapore 117543[1]
MajuLab, CNRS-UNS-NUS-NTU International Joint Research Unit UMI 3654, Singapore 117543[2]
Clarendon Laboratory, University of Oxford, Parks Road, Oxford OX1 3PU, United Kingdom[3] *and*
Department of Physics, National University of Singapore, 117542, Singapore[4]

PACS numbers: 42.50.Gy,42.65.Ky,32.80.Ee

I. THEORY

The numerical simulations presented in the main text are performed within the framework of the Maxwell-Bloch equations, with the central relations derived in Sec. I A. The input parameters for the simulation results are given in Sec. I B, and Sec. I C discusses the details of the dark state mentioned in connection with Fig. 3 of the main text. Finally, details about the simulation for co-propagating microwave and optical fields are described in Sec. I D.

A. Maxwell-Bloch equations

We model the interaction of all microwave and laser fields with the atomic ensemble within the standard framework of coupled Maxwell-Bloch equations. Due to the low atomic density and small Rydberg populations, interactions between Rydberg atoms are weak and are described by effective dephasing rates in the single-atom picture. We decompose all electric fields as

$$\boldsymbol{E}_{\mathrm{X}} = \boldsymbol{E}_{\mathrm{X}}^{(+)}(\boldsymbol{r},t) + \text{c.c.}\,, \tag{S1}$$

where $\boldsymbol{E}_{\mathrm{X}}^{(+)}$ is the positive frequency part of field X ($\mathrm{X} \in \{\mathrm{P},\mathrm{C},\mathrm{A},\mathrm{M},\mathrm{R},\mathrm{L}\}$). The positive frequency part of $\boldsymbol{E}_{\mathrm{X}}$ is written as

$$\boldsymbol{E}_{\mathrm{X}}^{(+)}(\boldsymbol{r},t) = \boldsymbol{e}_{\mathrm{X}}\mathcal{E}_{\mathrm{X}}(\boldsymbol{r},t)\; e^{\mathrm{i}(\boldsymbol{k}_{\mathrm{X}}\cdot\boldsymbol{r}-\omega_{\mathrm{X}}t)}\,, \tag{S2}$$

where $\boldsymbol{e}_{\mathrm{X}}$ is the unit polarisation vector, ω_{X} is the central frequency, $\boldsymbol{k}_{\mathrm{X}}$ is the wave vector and $\mathcal{E}_{\mathrm{X}}$ is the envelope function of field $\boldsymbol{E}_{\mathrm{X}}$. The master equation describing the quantum dynamics of the single-atom density operator ϱ can be written as

$$\partial_t\varrho = -\frac{i}{\hbar}[H,\varrho] + \mathcal{L}_{\gamma}\varrho + \mathcal{L}_{\mathrm{deph}}\varrho\,, \tag{S3}$$

where H is the Hamiltonian for a single atom interacting with the six external fields. In the electric-dipole and rotating-wave approximation, we find

$$\begin{aligned} H = &-\hbar\,[\Delta_{\mathrm{P}}A_{22} + (\Delta_{\mathrm{P}}+\Delta_{\mathrm{C}})A_{33} \\ &\quad+(\Delta_{\mathrm{P}}+\Delta_{\mathrm{C}})A_{44} + (\Delta_{\mathrm{P}}+\Delta_{\mathrm{C}}+\Delta_{\mathrm{M}})A_{55} \\ &\quad+(\Delta_{\mathrm{P}}+\Delta_{\mathrm{C}}+\Delta_{\mathrm{M}})A_{66}] \\ &-\frac{\hbar}{2}\,(\Omega_{\mathrm{P}}A_{21} + \Omega_{\mathrm{C}}A_{32} + \Omega_{\mathrm{A}}A_{34} \\ &\quad+\Omega_{\mathrm{M}}A_{54} + \Omega_{\mathrm{R}}A_{56} + \Omega_{\mathrm{L}}A_{61} + \text{H.c.})\,, \end{aligned} \tag{S4}$$

where $A_{ij} = |i\rangle\langle j|$ are atomic transition operators between the states introduced in Fig. 1(a) of the main text. In the derivation of Eq. (S4) we assumed that the six microwave and laser fields drive a resonant loop,

$$\omega_{\mathrm{P}} + \omega_{\mathrm{C}} + \omega_{\mathrm{M}} - \omega_{\mathrm{R}} - \omega_{\mathrm{A}} - \omega_{\mathrm{L}} = 0\,. \tag{S5}$$

Furthermore, we assumed that the phase matching condition

$$\boldsymbol{k}_{\mathrm{L}} = \boldsymbol{k}_{\mathrm{P}} + \boldsymbol{k}_{\mathrm{C}} + \boldsymbol{k}_{\mathrm{M}} - \boldsymbol{k}_{\mathrm{R}} - \boldsymbol{k}_{\mathrm{A}} \tag{S6}$$

is fulfilled. The detuning parameters Δ_{P}, Δ_{C} and Δ_{M} in Eq. (S4) are defined as

$$\Delta_{\mathrm{P}} = \omega_{\mathrm{P}} - \omega_{21}\,, \tag{S7a}$$

$$\Delta_{\mathrm{C}} = \omega_{\mathrm{C}} - \omega_{32}\,, \tag{S7b}$$

$$\Delta_{\mathrm{M}} = \omega_{\mathrm{M}} - \omega_{54}\,, \tag{S7c}$$

where ω_{kj} is the transition frequency between levels $|k\rangle$ and $|j\rangle$. The Rabi frequencies of the various fields are

$$\Omega_{\mathrm{P}} = 2\frac{\boldsymbol{d}_{21}\cdot\boldsymbol{e}_{\mathrm{P}}}{\hbar}\mathcal{E}_{\mathrm{P}}, \tag{S8a}$$

$$\Omega_{\mathrm{C}} = 2\frac{\boldsymbol{d}_{32}\cdot\boldsymbol{e}_{\mathrm{C}}}{\hbar}\mathcal{E}_{\mathrm{C}}, \tag{S8b}$$

$$\Omega_{\mathrm{A}} = 2\frac{\boldsymbol{d}_{34}\cdot\boldsymbol{e}_{\mathrm{A}}}{\hbar}\mathcal{E}_{\mathrm{A}}, \tag{S8c}$$

$$\Omega_{\mathrm{M}} = 2\frac{\boldsymbol{d}_{54}\cdot\boldsymbol{e}_{\mathrm{M}}}{\hbar}\mathcal{E}_{\mathrm{M}}, \tag{S8d}$$

$$\Omega_{\mathrm{R}} = 2\frac{\boldsymbol{d}_{56}\cdot\boldsymbol{e}_{\mathrm{R}}}{\hbar}\mathcal{E}_{\mathrm{R}}, \tag{S8e}$$

$$\Omega_{\mathrm{L}} = 2\frac{\boldsymbol{d}_{61}\cdot\boldsymbol{e}_{\mathrm{L}}}{\hbar}\mathcal{E}_{\mathrm{L}}, \tag{S8f}$$

and

$$\boldsymbol{d}_{kl} = \langle k|\hat{\boldsymbol{d}}|l\rangle \tag{S9}$$

is the matrix element of the electric dipole moment operator $\hat{\boldsymbol{d}}$ on the transition $|k\rangle \leftrightarrow |l\rangle$. The term $\mathcal{L}_\gamma \varrho$ in Eq. (S3) accounts for spontaneous emission of the excited states that we describe by standard Lindblad decay terms,

$$\begin{aligned}\mathcal{L}_\gamma \varrho = &-\frac{\Gamma}{2}\left(A_{22}\varrho + \varrho A_{22} - 2A_{12}\varrho A_{12}^\dagger\right)\\ &-\frac{\Gamma}{2}\left(A_{66}\varrho + \varrho A_{66} - 2A_{16}\varrho A_{16}^\dagger\right)\\ &-\frac{\gamma_r}{2}\left(A_{33}\varrho + \varrho A_{33} - 2A_{23}\varrho A_{23}^\dagger\right)\\ &-\frac{\gamma_r}{2}\left(A_{55}\varrho + \varrho A_{55} - 2A_{65}\varrho A_{65}^\dagger\right)\\ &-\frac{\gamma_{r'}}{2}\left(A_{44}\varrho + \varrho A_{44} - 2A_{14}\varrho A_{14}^\dagger\right) . \end{aligned} \tag{S10}$$

In this equation, Γ is the full decay rate of states $|2\rangle$ and $|6\rangle$ that decay back to the ground state $|1\rangle$. The terms proportional to γ_r, $\gamma_{r'} \ll \Gamma$ in Eq. (S10) account for the decay of the meta-stable Rydberg states $|3\rangle$, $|4\rangle$ and $|5\rangle$. More specifically, γ_r is the decay rate of states $|3\rangle$ and $|5\rangle$, and $\gamma_{r'}$ corresponds to that of state $|4\rangle$. The latter terms represent a simplified model for the decay of Rydberg states, which in general decay to various lower-lying states outside our simple six-level model via cascades assisted by blackbody radiation [S1]. However, we find that our results do not depend on the details of the Rydberg decay terms since γ_r and $\gamma_{r'}$ are by far the smallest frequencies in our model (see Sec. I B).

The last term in Eq. (S3) accounts for dephasing of atomic coherences due to finite laser linewidths, atomic collisions and dipole-dipole interactions between Rydberg atoms,

$$\begin{aligned}\mathcal{L}_{\text{deph}}\varrho = &-\gamma_d\left(A_{33}\varrho + \varrho A_{33} - 2A_{33}\varrho A_{33}\right)\\ &-\gamma_d'\left(A_{55}\varrho + \varrho A_{55} - 2A_{55}\varrho A_{55}\right)\\ &-\gamma_{DD}\left(A_{44}\varrho + \varrho A_{44} - 2A_{44}\varrho A_{44}\right) . \end{aligned} \tag{S11}$$

The dephasing rates γ_d, γ_d' and γ_{DD} are free parameters and are obtained from a fit to experimental data as described in Sec. III E.

We only treat fields P and L in a self-consistent way and assume that the depletion of the other fields is small. The propagation of the P and L fields inside the medium is governed by Maxwell's equations. In the paraxial approximation we find

$$\left(-\frac{\mathrm{i}}{2k_\mathrm{P}}\Delta_\perp + \frac{1}{c}\partial_t + \partial_z\right)\Omega_\mathrm{P} = 2\mathrm{i}\eta_\mathrm{P}\varrho_{21} , \tag{S12a}$$

$$\left(-\frac{\mathrm{i}}{2k_\mathrm{L}}\Delta_\perp + \frac{1}{c}\partial_t + \partial_z\right)\Omega_\mathrm{L} = 2\mathrm{i}\eta_\mathrm{L}\varrho_{61} , \tag{S12b}$$

where k_P (k_L) is the wavenumber of the P (L) field and $\Delta_\perp = \partial_x^2 + \partial_y^2$ is the transverse Laplace operator. The coupling constants η_P and η_L are given by

$$\eta_\mathrm{P} = \frac{n_\mathrm{at}|\boldsymbol{d}_{21}|^2}{2\hbar\epsilon_0 c}\omega_\mathrm{P} , \tag{S13a}$$

$$\eta_\mathrm{L} = \frac{n_\mathrm{at}|\boldsymbol{d}_{61}|^2}{2\hbar\epsilon_0 c}\omega_\mathrm{L} , \tag{S13b}$$

and c is the speed of light. The set of equations (S3) and (S12) represent a system of coupled, partial differential equations and have to be solved consistently for given initial and boundary conditions. We numerically find the steady-state solution of Eqs. (S3) and (S12) with MATHEMATICA [S2] and the implicit differential-algebraic solver (IDA) method option for NDSolve.

B. Input parameters

We assume that the fields C and R are unaffected by the interaction with the atoms and thus take the free-space solutions of Maxwell's equations in paraxial approximation in order to describe their spatial profile. Fields C and R propagate in $-z$ direction and are given by

$$\Omega_\mathrm{C}(z,r) = \Omega_\mathrm{C}^{(0)}\frac{\mathrm{i}z_\mathrm{C}}{z+\mathrm{i}z_\mathrm{C}}e^{-\mathrm{i}z_\mathrm{C}r^2/[w_\mathrm{C}^2(z+\mathrm{i}z_\mathrm{C})]} , \tag{S14a}$$

$$\Omega_\mathrm{R}(z,r) = \Omega_\mathrm{R}^{(0)}\frac{\mathrm{i}z_\mathrm{R}}{z+\mathrm{i}z_\mathrm{R}}e^{-\mathrm{i}z_\mathrm{R}r^2/[w_\mathrm{R}^2(z+\mathrm{i}z_\mathrm{R})]} , \tag{S14b}$$

where z_C (z_R) is the Rayleigh length and w_C (w_R) is the beam waist of field C (R) at $z=0$, and $\Omega_\mathrm{C}^{(0)}$ ($\Omega_\mathrm{R}^{(0)}$) is the peak Rabi frequency at the center of the beam waist of field C (R). In Eq. (S14), $r=\sqrt{x^2+y^2}$ denotes the radial distance from the z axis. The microwave fields M and A are assumed to be constant throughout the atomic sample. We model the density profile of the atomic cloud in z direction by

$$n_\mathrm{at}(z) = \tilde{n}_\mathrm{at}e^{-2(z/w_z)^2}\theta(z+z_\mathrm{max})\theta(z_\mathrm{max}-z) , \tag{S15}$$

where $\theta(z)$ is the Heaviside step function, $z_\mathrm{max} = 1.5w_z$ and w_z is the $1/e^2$ radius of the Gaussian density profile. For a given optical depth D_P and cloud radius w_z, the peak atomic density $\tilde{n}_\mathrm{at}$ in Eq. (S15) is determined by

$$\tilde{n}_\mathrm{at} = \frac{D_\mathrm{P}\Gamma}{4\bar{\eta}}\left(\int_{-z_\mathrm{max}}^{z_\mathrm{max}} e^{-2(z/w_z)^2}\mathrm{d}z\right)^{-1} , \tag{S16}$$

where $\bar{\eta} = \omega_\mathrm{P}|\boldsymbol{d}_{21}|^2/(2\hbar\epsilon_0 c)$.

The P field is focussed at the center of the atomic cloud at $z=0$ and propagates in z direction. The initial condition for the P field in the $x-y$ plane at the entrance of the medium at $-z_\mathrm{max}$ is thus given by

$$\Omega_\mathrm{P}(-z_\mathrm{max},r) = \Omega_\mathrm{P}^{(0)}\frac{\mathrm{i}z_\mathrm{P}}{z_\mathrm{max}+\mathrm{i}z_\mathrm{P}}e^{-\mathrm{i}z_\mathrm{P}r^2/[w_\mathrm{P}^2(z_\mathrm{max}+\mathrm{i}z_\mathrm{P})]} , \tag{S17}$$

where z_P is the Rayleigh length and w_P is the beam waist of field P. The corresponding initial condition for Ω_L is $\Omega_\mathrm{L}(-z_\mathrm{max},r)=0$.

The simulation results presented in the main text are obtained with the following parameters:

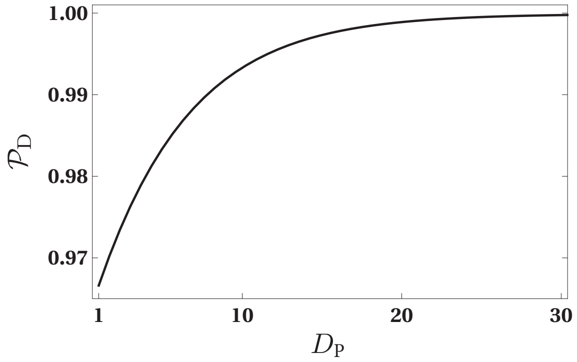

FIG. S1. Probability $\mathcal{P}_\mathrm{D}$ for the atoms at the center of the atomic cloud to be in the dark state $|D\rangle$. The parameters correspond to those of Fig. 4 in the main text.

- Fig. 2: Δ_P is varied. $\Omega_\mathrm{C}^{(0)} = 2\pi \times 9.04\,\mathrm{MHz}$, $\Omega_\mathrm{R}^{(0)} = 2\pi \times 6.2\,\mathrm{MHz}$, $\Omega_\mathrm{P}^{(0)} = 2\pi \times 1.14\,\mathrm{MHz}$, $\Omega_\mathrm{M} = 2\pi \times 1.25\,\mathrm{MHz}$, $\Omega_\mathrm{A} = 2\pi \times 1.06\,\mathrm{MHz}$, $\Delta_\mathrm{M} = 0$, $\Delta_\mathrm{C} = -2\pi \times 0.1\,\mathrm{MHz}$ and $D_\mathrm{P} = 14.0$.

- Fig. 3: D_P is varied. $\Omega_\mathrm{C}^{(0)} = 2\pi \times 9.04\,\mathrm{MHz}$, $\Omega_\mathrm{R}^{(0)} = 2\pi \times 6.2\,\mathrm{MHz}$, $\Omega_\mathrm{P}^{(0)} = 2\pi \times 1.14\,\mathrm{MHz}$, $\Omega_\mathrm{M} = 2\pi \times 1.25\,\mathrm{MHz}$, $\Omega_\mathrm{A} = 2\pi \times 1.06\,\mathrm{MHz}$, $\Delta_\mathrm{P} = 0$, $\Delta_\mathrm{M} = 0$ and $\Delta_\mathrm{C} = -2\pi \times 0.1\,\mathrm{MHz}$.

- Fig. 4: Δ_M and Ω_M are varied. $\Omega_\mathrm{C}^{(0)} = 2\pi \times 9.04\,\mathrm{MHz}$, $\Omega_\mathrm{R}^{(0)} = 2\pi \times 6.2\,\mathrm{MHz}$, $\Omega_\mathrm{P}^{(0)} = 2\pi \times 1.14\,\mathrm{MHz}$, $\Omega_\mathrm{A} = 2\pi \times 1.06\,\mathrm{MHz}$, $\Delta_\mathrm{P} = 0$, $\Delta_\mathrm{C} = 0$ and $D_\mathrm{P} = 14.3$.

The values for these parameters are taken from experimental measurements and calibrations. Common parameters for all three figures are $\Gamma = 2\pi \times 6.067\,\mathrm{MHz}$, $\gamma_r = 1.53 \times 10^{-3}\Gamma$, $\gamma_{r'} = 1.02 \times 10^{-3}\Gamma$, $\gamma_d = 2\pi \times 0.15\,\mathrm{MHz}$, $\gamma_d' = 2\pi \times 0.56\,\mathrm{MHz}$ and $\gamma_{DD} = 2\pi \times 0.15\,\mathrm{MHz}$. Here Γ is the decay rate of the $5\mathrm{P}_{3/2}$ state [S3], γ_r corresponds to the decay rate of the 30D states and $\gamma_{r'}$ is the decay rate of the 31P state. The values for the Rydberg decay rates are taken from [S4, S5] and correspond to an ambient temperature of 300 K.

C. Dark state

Here we show that the Hamiltonian in Eq. (S4) exhibits a so-called dark state $|D\rangle$ [S6]. For $\Delta_\mathrm{P} = \Delta_\mathrm{L} = \Delta_\mathrm{M} = 0$ and

$$\Omega_\mathrm{L}/\Omega_\mathrm{P} = -\frac{\Omega_\mathrm{A}^*\Omega_\mathrm{R}^*}{\Omega_\mathrm{M}^*\Omega_\mathrm{C}^*}\,, \tag{S18}$$

one of the eigenstates of H takes the form

$$|D\rangle = \mathcal{C}\left(\Omega_\mathrm{M}^*\Omega_\mathrm{C}^*|1\rangle - \Omega_\mathrm{M}^*\Omega_\mathrm{P}|3\rangle + \Omega_\mathrm{A}^*\Omega_\mathrm{P}|5\rangle\right)\,, \tag{S19}$$

and the normalisation constant is

$$\mathcal{C} = \frac{1}{\sqrt{\Omega_\mathrm{A}^2\Omega_\mathrm{P}^2 + \Omega_\mathrm{M}^2(\Omega_\mathrm{P}^2 + \Omega_\mathrm{C}^2)}}\,. \tag{S20}$$

The eigenstate $|D\rangle$ has non-zero population only in states $|1\rangle$, $|3\rangle$ and $|5\rangle$ that are all meta-stable. The density operator

$$\varrho_\mathrm{D} = |D\rangle\langle D| \tag{S21}$$

is thus an approximately stationary solution to the master equation (S3), $\partial_t\varrho_\mathrm{D} \approx 0$. Furthermore, all the matrix elements of ϱ_D between allowed dipole transitions of our atomic level scheme vanish, and hence atoms in this state are decoupled from all six fields.

We calculate the probability for the atoms to be in state $|D\rangle$ by

$$\mathcal{P}_\mathrm{D} = \left(\mathrm{Tr}\left[\sqrt{\sqrt{\varrho_\mathrm{D}}\varrho\sqrt{\varrho_\mathrm{D}}}\right]\right)^2\,, \tag{S22}$$

where ϱ is the steady-state solution of Eq. (S3) at a given position (z, r) in space. The result for atoms at the center of the cloud at $r = 0$ is shown in Fig. S1. We find that $\mathcal{P}_\mathrm{D}$ increases with optical depth, and $\mathcal{P}_\mathrm{D} \approx 99.86\,\%$ at $D_\mathrm{P} = 20$.

D. Co-propagating fields

The good agreement between our model in Sec. I A and the experimental data allows us to theoretically explore the case where the microwave fields M and A are co-propagating with the P field. In this case, we also treat the M field in a self-consistent way. In paraxial approximation, the propagation of the M field is governed by

$$\left(-\frac{\mathrm{i}}{2k_\mathrm{M}}\Delta_\perp + \frac{1}{c}\partial_t + \partial_z\right)\Omega_\mathrm{M} = 2\mathrm{i}\eta_\mathrm{M}\varrho_{21}\,, \tag{S23}$$

where k_M is the wavenumber of the M field and

$$\eta_\mathrm{M} = \frac{n_\mathrm{at}|\boldsymbol{d}_{54}|^2}{2\hbar\epsilon_0 c}\omega_\mathrm{M} \tag{S24}$$

is the coupling constant. The initial condition for the M field in the $x - y$ plane at $-z_\mathrm{max}$ is

$$\Omega_\mathrm{M}(-z_\mathrm{max}, r) = \Omega_\mathrm{M}^{(0)}\frac{\mathrm{i}z_\mathrm{M}}{z_\mathrm{max} + \mathrm{i}z_\mathrm{M}}e^{-\mathrm{i}z_\mathrm{M}r^2/[w_\mathrm{M}^2(z_\mathrm{max}+\mathrm{i}z_\mathrm{M})]}\,, \tag{S25}$$

where z_M is the Rayleigh length and w_M is the beam waist of field M. We assume that $w_\mathrm{M} = 5\,\mathrm{mm}$ is larger than the wavelength $\lambda_\mathrm{M} \approx 3.6\,\mathrm{mm}$ of field M in order to be consistent with the paraxial approximation. The peak Rabi frequency is $\Omega_\mathrm{M}^{(0)} = 2\pi \times 0.61\,\mathrm{MHz}$ and we set $\Delta_\mathrm{M} = 0$. Note that $w_\mathrm{M} \gg w_\mathrm{P}$ and thus the microwave intensity is approximately constant over the transverse beam profile of the P field. With all other parameters as in Fig. 4 we find that the conversion efficiency is $\eta^\parallel \approx 0.26$ in this geometry.

II. EXPERIMENTAL DETAILS

A. Electric transition dipole moments and fields intensities

In the six-wave mixing scheme of Fig. 1(a), each electric dipole transition is coupled to one given field X. Below, we list for each transition the respective electric transition dipole moment, the field X to which it couples to, and if applicable the estimated peak intensity and waist of field X based on calibrations given in Sec. III.

TABLE I. Relevant electric transition dipole moments $|\boldsymbol{d}_{kl}|$, field intensities, and waists. $|\boldsymbol{d}_{kl}|$ is given in the units of $e\,a_0$, where e is the elementary charge, and a_0 is the Bohr radius.

Transition	$\lvert\boldsymbol{d}_{kl}\rvert$ (in units of $e\,a_0$)	Field	Peak intensity (W m^{-2})	Waist (μm)
$\|1\rangle \leftrightarrow \|2\rangle$	2.99	P	1.15	24.8
$\|2\rangle \leftrightarrow \|3\rangle$	0.0138	C	$8.0\ \times 10^{6}$	53.8
$\|3\rangle \leftrightarrow \|4\rangle$	74.5	A	$1.35\ \times 10^{-3}$	NA
$\|4\rangle \leftrightarrow \|5\rangle$	546.8	M	NA	NA
$\|5\rangle \leftrightarrow \|6\rangle$	0.00914	R	$1.7\ \times 10^{6}$	45.4
$\|1\rangle \leftrightarrow \|6\rangle$	1.22	L	NA	NA

B. Numerical phase detection

The beat signal to be demodulated is of the form

$$f(t) = A_0 + A\cos\left(2\pi f_c t + \phi\left(t\right)\right),$$

where A_0 is a constant, A is the amplitude of the beat note, $f_c = 9.5517$ MHz is the center frequency, and $\phi\left(t\right)$ is the phase to be recovered. The numerical demodulation and phase detection are done by first multiplying the beat note $f(t)$ with the complex exponential function of frequency f_c, then applying a low-pass Fourier filter (convolution product in time domain with the impulse response of the filter Kern(t)), and finally recovering the phase $\phi(t)$:

$$\begin{aligned} f(t) &\leftarrow f(t)\ e^{-i2\pi f_c t} \\ f(t) &\leftarrow f(t) * \mathrm{Kern}(t) \\ \phi(t) &\leftarrow \mathrm{Arg}\left[f(t)\right] \\ \phi(t) &\leftarrow \mathrm{Unwrap}\left[\phi(t)\right], \end{aligned}$$

The Fourier filtering corresponds to a low-pass filter of 300 kHz cutoff frequency. Arg computes the phase in radians in the interval $]-\pi,\pi]$, and the result of the phase detection is unwrapped such that it does not show unphysical phase jumps of 2π in the case where $\phi\left(t\right)$ lies outside this interval.

III. CALIBRATION OF THE EXPERIMENTAL PARAMETERS

A. General method

Many of our experimental parameters are extracted from fitting the spectra of the P field power transmitted through the atomic cloud versus Δ_{P}, where Δ_{P} is the detuning of the P field, as defined by Eq. (S7a). The transmission spectra are recorded as $T\left(\Delta_P\right) = P_{\mathrm{P,out}}/P_{\mathrm{P,in}}$, where $P_{\mathrm{P,in}}$ and $P_{\mathrm{P,out}}$ are the input and output P field powers. The experimental conditions for these calibrations are similar to the ones reported in the main text for the actual six-wave mixing experiment, except that only the fields relevant to each parameter calibration are used in the measurements, as described in the next subsections.

The transmission spectra are recorded with P field intensities I_{P} much smaller than the saturation intensity $I_{\mathrm{S}} = 16.69$ Wm^{-2} of the $|1\rangle \leftrightarrow |2\rangle$ transition [S3]. Thus the atomic coherence ϱ_{21} in Eq. (S12a) may be replaced by its approximation calculated at first order in Ω_{P}, which we write as $\varrho_{21} \approx \varsigma_{21}^{(1)}\Omega_{\mathrm{P}}$, where $\varsigma_{21}^{(1)}$ is the first order Taylor coefficient. Furthermore, the spatial profile of the P field in the transverse dimension is much narrower than the C and R fields, but still relatively well collimated. We shall write the P field in steady state as $\mathcal{E}_{\mathrm{P}}(r,z) = \mathcal{E}_{\mathrm{P,in}}(r,0)\ f(r,z)$, where $\mathcal{E}_{\mathrm{P,in}}(r,0)$ denotes the P field in absence of atoms at $z = 0$. To a good approximation, we will neglect the transverse Laplacian $\Delta_{\perp}\mathcal{E}_{\mathrm{P}}(r,z)$ in Eq. (S12a), hence obtain a one-dimensional linear differential equation satisfied by $f(r,z)$. This last assumption is confirmed by the quasi absence of lensing effects in the calibration experiments [S7]. Eventually, those different approximations lead to the following equation, used for fitting the P field transmission spectra as in Ref. [S8]

$$T = \frac{1}{\mathcal{N}}\int_0^{+\infty} 2\pi r\left|\mathcal{E}_{\mathrm{P,in}}(r,0)\right|^2 \exp\left(-D_{\mathrm{P}}\ \mathrm{Im}\left[\frac{k_{\mathrm{P}}^3}{6\pi}\alpha\left(r\right)\right]\right)\mathrm{d}r, \tag{S26}$$

where D_{P} is the optical depth, $\alpha\left(r\right)$ refers to the linear polarizability, and $\mathcal{N} = \int_0^{+\infty}|\mathcal{E}_{\mathrm{P,in}}(r,0)|^2 2\pi r \mathrm{d}r$. The optical depth is proportional to the column density, and writes

$$D_{\mathrm{P}} = \frac{6\pi}{k_{\mathrm{P}}^2}\int_{-\infty}^{+\infty} n_{at}(z)dz, \tag{S27}$$

while the linear polarizability is given by [S9]

$$\alpha\left(r\right) = \frac{6\pi}{k_{\mathrm{P}}^3}\Gamma\varsigma_{21}^{(1)}\left(r\right). \tag{S28}$$

Eq. (S26) is used as a fitting formula for most of our calibrations. The calibrations are performed sequentially with increasing number of input fields in order to limit the number of free fitting parameters, as shown in the following subsections. The calibrations of the laser waists w_{P}, w_{C}, and w_{R} are performed with imaging techniques as described in Ref. [S7], and will not be discussed in this section.

B. Optical depth D_{P}

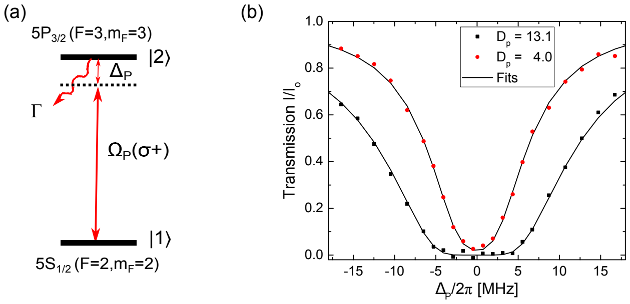

FIG. S2. (a) Two-level scheme for the measurement of the optical depth D_{P}. The P field of σ^+ polarization drives the transition from the ground state $|5S_{1/2}, F=2, m_F=2\rangle$ ($|1\rangle$) to the excited state $|5P_{3/2}, F=3, m_F=3\rangle$ ($|2\rangle$). (b) Typical spectra showing the power transmission of the P field versus Δ_{P} and fitting curves. The P field transmission is recorded versus detuning Δ_{P} with Rabi frequency $\Omega_{\mathrm{P}}^{(0)} = 2\pi \times 0.46 \pm 0.03$ MHz. The two spectra are taken with atomic samples which have the same $1/e^2$ radius $w_z = 1.85 \pm 0.1$ mm but different atomic densities (see main manuscript for the preparation). The solid lines are fits to Eq. (S29).

The optical depth D_{P} is extracted directly from the two-level transmission spectra, obtained when only the P field is sent onto the atoms. In this case, the polarizability α is independent of r and the fitting formula (S26) reduces to

$$T\left(D_{\mathrm{P}}, \Delta_{\mathrm{P}}\right) = \exp\left(-\frac{D_{\mathrm{P}}}{1+\frac{4\Delta_{\mathrm{P}}^2}{\Gamma^2}}\right). \tag{S29}$$

Two sample spectra and fits to Eq. (S29) are shown in Fig. S2, that provide calibrations for the optical depth D_{P}, and also for the position of the centerline laser frequency where $\Delta_{\mathrm{P}} = 0$, i.e. $\omega_{\mathrm{P}} = \omega_{21}$. The results of the fits show that the optical depth of the two corresponding atomic samples are $D_P = 13.1 \pm 0.3$ and $D_P = 4.0 \pm 0.2$.

C. Dephasing of the EIT spectra γ_d and Rabi frequency Ω_{C}

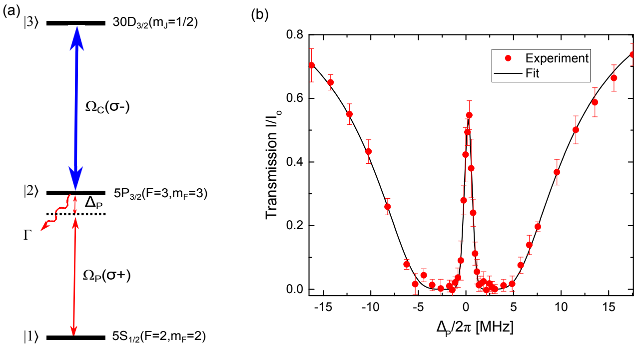

FIG. S3. (a) Three-level scheme for the measurement of the Rabi frequency $\Omega_{\mathrm{C}}^{(0)}$. The C field of σ^- polarization drives the transition from the $|5P_{3/2}, F=3, m_F=3\rangle$ ($|2\rangle$) state to $|30D_{3/2}, m_J=1/2\rangle$ ($|3\rangle$), and Ω_{C} is the Rabi frequency of the C field, while other features of the excitation scheme are similar to that of Fig. S2. (b) Typical spectrum showing the power transmission of the P field versus Δ_{P} and fitting curve. The P field transmission is recorded versus detuning Δ_{P}. The spectrum is taken with the following experimental conditions: optical depth $D_{\mathrm{P}} = 10.1 \pm 0.2$; peak atomic density $n_0 = 1.7 \pm 0.2 \times 10^{10}$ cm^{-3}; $1/e^2$ radius of the atomic cloud $w_z = 1.6 \pm 0.2$ mm; $\Omega_{\mathrm{P}}^{(0)} = 2\pi \times 0.42 \pm 0.03$ MHz. The solid line is a fit to Eq. (S26).

When we add the coupling field C to the previous two-level excitation scheme, the recorded transmission spectra are typical of electromagnetically induced transparency (EIT), as illustrated in Fig. S3, with a transmission peak that occurs when the resonance condition $\Delta_{\mathrm{P}} + \Delta_{\mathrm{C}} = 0$ is satisfied [S10]. In this three-level case, the polarizability entering Eq. (S26) writes [S11]

$$\alpha\left(r\right) = \frac{3\pi}{k_{\mathrm{P}}^3} \frac{i\Gamma}{\frac{\Gamma}{2} - i\Delta_{\mathrm{P}} + \frac{\Omega_{\mathrm{C}}^2(r)/4}{\gamma_d - i(\Delta_{\mathrm{P}}+\Delta_{\mathrm{C}})}}, \tag{S30}$$

where $\Omega_{\mathrm{C}}\left(r\right)$ is given by Eq. (S14) at $z=0$. The fits of the EIT transmission spectra to Eq. (S26), with optical depth D_{P} as input parameter from the previous measurement, yield calibrations for γ_d, Δ_{C}, and the peak Rabi frequency $\Omega_{\mathrm{C}}^{(0)}$. In the particular case of Fig. S3, the results of the fit are $\gamma_d = 2\pi \times 0.11 \pm 0.015$ MHz, $\Delta_{\mathrm{C}} = -2\pi \times 0.26 \pm 0.15$ MHz and $\Omega_{\mathrm{C}}^{(0)} = 2\pi \times 5.0 \pm 0.15$ MHz. The dephasing rate γ_d varies depending on the various experimental parameters that affect the population in Rydberg state $|3\rangle$. If we acquired the EIT spectrum of Fig. S3 with experimental conditions as in Fig. 2 of the main text, we would obtain a larger value of $\gamma_d/2\pi$ in the range $0.15 - 0.2$ MHz, very similar to the value that will be obtained from fitting the six-wave mixing spectra in subsection III E.

The measurement of $\Omega_{\mathrm{R}}^{(0)}$ is done very similarly, while simply replacing the optical field C by the optical field R in the three-level scheme of Fig. S4(a). However, in this latter case, the optical frequency of the R field is tuned to drive the transition $|5P_{3/2}, F=3, m_F=3\rangle \leftrightarrow |30D_{5/2}, m_J=1/2\rangle$. As a result, we measure the Rabi frequency of the coupling of R field with the $|5P_{3/2}, F=3, m_F=3\rangle \leftrightarrow |30D_{5/2}, m_J=1/2\rangle$ transition. This Rabi coupling then needs to be multiplied by 1.22 in order to retrieve the Rabi coupling $\Omega_{\rm R}^{(0)}$ corresponding to the R field driving the transition $|5P_{3/2}, F = 2, m_F = 1\rangle \leftrightarrow |30D_{5/2}, m_J = 1/2\rangle$ in the actual six-wave mixing experiment.

D. Microwave field amplitude

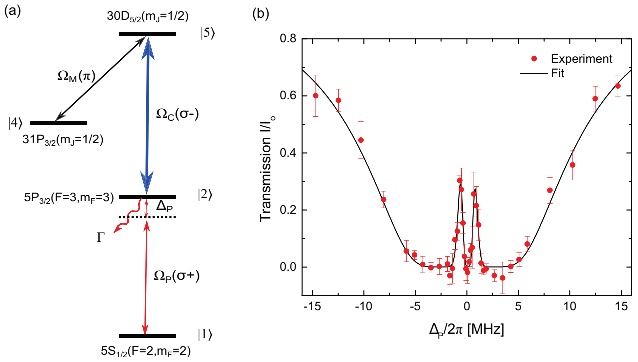

FIG. S4. (a) Four-level scheme for the measurement of the Rabi frequency of field M. The field M drives the transition from the Rydberg state $|30D_{5/2}, m_J = 1/2\rangle$ ($|5\rangle$) to the nearby Rydberg state $|31P_{3/2}, m_J = 1/2\rangle$ ($|4\rangle$), with a resonance frequency of about 83.714 GHz. The other features of the excitation scheme are similar to that of Fig. S3, except that the optical frequency of the C field is tuned to drive the transition $|2\rangle \leftrightarrow |30D_{5/2}, m_J = 1/2\rangle$ instead of $|2\rangle \leftrightarrow |30D_{3/2}, m_J = 1/2\rangle$. $\Omega_{\rm M}$ is the Rabi frequency associated with the microwave field. (b) Typical spectrum showing the power transmission of the P field versus $\Delta_{\rm P}$ and fitting curve (see text). The spectrum is taken with the following experimental conditions: optical depth $D_{\rm P} = 10.5 \pm 0.5$; peak atomic density $n_0 = 1.8 \pm 0.2 \times 10^{10}\,{\rm cm}^{-3}$; $1/e^2$ radius of the atomic cloud $w_z = 1.6 \pm 0.2$ mm; $\Omega_{\rm P}^{(0)} = 2\pi \times 0.41 \pm 0.03$ MHz; $\Omega_{\rm C}^{(0)} = 2\pi \times 5.2 \pm 0.15\,$MHz; $\Delta_{\rm C} = 2\pi \times -0.07 \pm 0.05\,$MHz; and $\Delta_{\rm M} = 2\pi \times 0.04 \pm 0.05\,$MHz. The solid line is a fit to Eq. (S26).

The microwave field amplitudes are calibrated by measuring the Rabi frequencies resulting from the electric-dipole coupling between the microwave fields and the relevant atomic transitions, as done for example in references [S8, S12–S14]. As given by Eqs. (S8d) and (S8c), the Rabi frequencies $\Omega_{\rm M}$ and $\Omega_{\rm A}$ are proportional to the respective field amplitudes $\mathcal{E}_{\rm M}$ and $\mathcal{E}_{\rm A}$ and the respective dipoles $|\boldsymbol{d}_{43}|$ and $|\boldsymbol{d}_{45}|$. We use the four-level EIT scheme of Fig. S4(a) for the particular measurement of the field M amplitude which is described in this subsection. The main idea is simply to fit the recorded spectra of the P field when both C and M fields are present.

A splitting of the transparency window appears in the spectra due to microwave dressing of the EIT dark state, as shown in Fig. S4. The parameters $D_{\rm P}$ and $\Omega_{\rm C}^{(0)}$ extracted previously from the spectra acquired without microwave field are taken as inputs when using Eq. (S26) to fit the data shown in Fig. S4. The free fit parameters are the microwave Rabi frequency $\Omega_{\rm M}$, the dephasing rates γ_d and γ_{DD}, introduced in Sec. I, and fields detunings. We obtain $\Omega_{\rm M} = 2\pi \times 1.33(10)$ MHz, $\gamma_{DD} = 2\pi \times 0.12(2)$ MHz, and $\gamma_d = 2\pi \times 0.13(2)$ MHz for the data of Fig. S4.

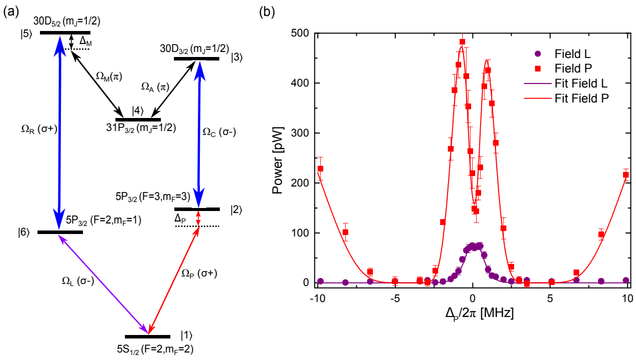

FIG. S5. (a) Six-level scheme for measuring the dephasing coefficient γ_{DD}. The field A drives the transition from the Rydberg state $|30D_{3/2}, m_J = 1/2\rangle$ ($|3\rangle$) to the Rydberg state $|31P_{3/2}, m_J = 1/2\rangle$ ($|4\rangle$) whose transition frequency is $\sim$ 0.454 GHz smaller than one of the $|5\rangle \rightarrow |4\rangle$ transition. The field R drives the transition from state $|5\rangle$ to $|5P_{3/2}, F = 2, m_F = 1\rangle$ ($|6\rangle$). The other features of the excitation scheme are similar to that of Fig. S4. $\Omega_{\rm M}$ is the Rabi frequency associated with the microwave field M, and $\Omega_{\rm R}$ that of the field R. (b) Typical spectra showing the optical powers of the transmitted P field and converted L field versus $\Delta_{\rm P}$ and fitting curves. The data are acquired with the following experimental conditions: optical depth $D_{\rm P} = 14.0 \pm 0.15$; peak atomic density $n_0 = 2.1 \pm 0.2 \times 10^{10}\,{\rm cm}^{-3}$; $1/e^2$ radius of the atomic cloud $w_z = 1.85 \pm 0.1$ mm ; $\Omega_{\rm P}^{(0)} = 2\pi \times 1.14 \pm 0.05$ MHz; $\Omega_{\rm C}^{(0)} = 2\pi \times 9.04 \pm 0.5\,$MHz; $\Delta_{\rm C} = 2\pi \times -0.1 \pm 0.1\,$MHz; $\Omega_{\rm R}^{(0)} = 2\pi \times 6.2 \pm 0.3\,$MHz; $\Delta_{\rm R} = 2\pi \times 0 \pm 0.5$MHz; $\Omega_{\rm A} = 2\pi \times 1.0 \pm 0.1\,$MHz; $\Omega_{\rm M} = 2\pi \times 1.25 \pm 0.12\,$MHz; $\Delta_{\rm A} = 2\pi \times 0 \pm 0.05\,$MHz; and $\Delta_{\rm M} = 2\pi \times 0 \pm 0.05\,$MHz. The fitting curve is obtained from the three-dimensional simulation.

The measurement is done very similarly for the microwave field A. For this purpose, the optical frequency of the C field is tuned to drive the transition $|2\rangle \leftrightarrow |30D_{3/2}, m_J = 1/2\rangle$ instead of $|2\rangle \leftrightarrow |30D_{5/2}, m_J = 1/2\rangle$ in the scheme of Fig. S4(a), while the A field drives the $|30D_{3/2}, m_J = 1/2\rangle \leftrightarrow |31P_{3/2}, m_J = 1/2\rangle$ transition.

E. Dephasing rates γ_d, γ_{DD}, and γ_d'

The dephasing rates, γ_d, γ_{DD}, and γ_d', are introduced in Sec. I in order to simulate the effects of interaction induced level shifts due to van der Waals or resonant dipole-dipole interactions. The calibration of these parameters used for the simulation of the six-wave mixing experiment are performed with the actual experimental conditions described in the main manuscript. More precisely, they are extracted from fitting the P and L fields spectra shown in Fig. S5(b)[Fig.2 (a) of the main text]. The calculations for the fit are carried out with the model described in Sec. I. γ_d, γ_{DD}, and γ_d' are left as free fit parameters in the fitting procedure, while all the other parameters are known inputs to the calculation. The fit result shown in Fig. S5 yields $\gamma_d = 2\pi \times 0.15$ MHz, $\gamma_{DD} = 2\pi \times 0.15$ MHz, and $\gamma_d' = 2\pi \times 0.56$ MHz. We find that these dephasing rates do not vary much in the parameter range relevant to the experiment, and hence we keep their values constant in all the other simulations reported in the main manuscript. The value for γ_d is similar to that found in subsection S3, which is consistent with the fact that resonant dipole-dipole interactions on the transition $|3\rangle \leftrightarrow |4\rangle$ are rather weak, hence do not affect much the transmission of the P field.

[S1] T. F. Gallagher, *Rydberg Atoms* (Cambridge University Press, Cambridge, 1994).

[S2] Wolfram Research, Inc., *Mathematica Version 10.1* (Wolfram Research, Inc., Irvine, Champaign, Illinois).

[S3] Daniel A. Steck, “Rubidium 87 D Line Data,” available online at `http://steck.us/alkalidata` (revision 2.1.4, 23 December 2010).

[S4] I. I. Beterov, I. I. Ryabtsev, D. B. Tretyakov, and V. M. Entin, Phys. Rev. A **79**, 052504 (2009).

[S5] D. B. Branden, T. Juhasz, T. Mahlokozera, C. Vesa, R. O. Wilson, M. Zheng, A. Kortyna, and D. A. Tate, Journal of Physics B: atomic, molecular and optical physics **43**, 015002 (2010).

[S6] E. Arimondo, in E. Wolf (Ed.), Progress in Optics, Vol. **35**, pp. 258, Elsevier, Amsterdam (1996).

[S7] J. Han, T. Vogt, M. Manjappa, R. Guo, M. Kiffner, and W. Li, Phys. Rev. A **92**, 063824 (2015).

[S8] M. Tanasittikosol, J. Pritchard, D. Maxwell, A. Gauguet, K. Weatherill, R. Potvliege, and C. Adams, Journal of Physics B: Atomic, Molecular and Optical Physics **44**, 184020 (2011).

[S9] G. Grynberg, A. Aspect, and C. Fabre, *Introduction to quantum optics: from the semi-classical approach to quantized light* (Cambridge university press, 2010).

[S10] M. Fleischhauer, A. Imamoğlu, and J. P. Marangos, Rev. Mod. Phys. **77**, 633 (2005).

[S11] J. Han, T. Vogt, and W. Li, Phys. Rev. A **94**, 043806 (2016).

[S12] J. A. Sedlacek, A. Schwettmann, H. Kübler, R. Löw, T. Pfau, and J. P. Shaffer, Nature Physics **8**, 819 (2012).

[S13] C. L. Holloway, J. A. Gordon, A. Schwarzkopf, D. A. Anderson, S. A. Miller, N. Thaicharoen, and G. Raithel, Applied Physics Letters **104**, 244102 (2014).

[S14] J. A. Gordon, C. L. Holloway, A. Schwarzkopf, D. A. Anderson, S. Miller, N. Thaicharoen, and G. Raithel, Applied Physics Letters **105**, 024104 (2014).